3-16-2022

Intermediate Temperature Solid Oxide Cell with a Barrier Layer Free Oxygen Electrode and Phase Inversion Derived Hydrogen Electrode

Yongliang Zhang

Nansheng Xu

Qiming Tang

Kevin Huang
University of South Carolina, huang46@cec.sc.edu

Publication Info

Published in *Journal of The Electrochemical Society*, Volume 169, Issue 3, 2022.

Journal of The Electrochemical Society

OPEN ACCESS

Intermediate Temperature Solid Oxide Cell with a Barrier Layer Free Oxygen Electrode and Phase Inversion Derived Hydrogen Electrode

To cite this article: Yongliang Zhang *et al* 2022 *J. Electrochem. Soc.* **169** 034516

Journal of The Electrochemical Society, 2022 **169** 034516

Intermediate Temperature Solid Oxide Cell with a Barrier Layer Free Oxygen Electrode and Phase Inversion Derived Hydrogen Electrode

Yongliang Zhang, Nansheng Xu, Qiming Tang, and Kevin Huang[*,z]

Department of Mechanical Engineering, University of South Carolina, Columbia, South Carolina 29201, United States of America

High-temperature solid oxide cells (SOCs) have fundamental advantages in efficiency and product rate over their low-temperature counterparts. However, the commercial development of SOCs is hindered by cost and reliability. To solve the issues, lowering the operating temperature of SOCs is deemed the best solution. Here we report on our effort toward intermediate temperature (IT) SOCs by developing a barrier layer free high-performance oxygen electrode and open structured hydrogen electrode. The results show that the new oxygen electrode provides reasonably good oxygen electrocatalytic activity at IT range for oxygen reduction and evolution reactions and the open structured hydrogen electrode provides low gas diffusion path for H_2/H_2O. However, at high electrolysis current density such as 1 A cm^{-2} and 650 °C, the present oxygen electrode delaminates after 200 h. The phase-inversion derived open structured hydrogen electrode helps gas diffusion but, in the meantime, reduces reactive sites. A proper balance of porosity and number of reactive sites is still needed for future hydrogen electrode development.
 [DOI: 10.1149/1945-7111/ac565a]

Manuscript submitted January 3, 2022; revised manuscript received February 2, 2022. Published March 16, 2022. *This paper is part of the JES Focus Issue on Focus Issue In Honor of John Goodenough: A Centenarian Milestone.*

High temperature solid oxide cell (SOC) technology is attracting considerable interest in recent decades for clean power generation and hydrogen production (green hydrogen) when combined with low-cost renewable energy. The key driver for such a strong interest is its superior thermodynamic efficiency and high-rate power and hydrogen production.[1] However, the current scale-up and commercialization efforts of SOCs are hindered by the insufficient durability and high cost, both of which are stemmed from the high operating temperature (700 °C–800 °C). A further reduction in operation temperature to, e.g. below 700 °C, is the best solution to address the durability and cost issues.[2] As the operating temperature is reduced, however, the resistances of cell components increase correspondingly. To decrease the resistances, one can use a thinner or higher conductivity electrolyte membrane, optimize the microstructure of fuel (or hydrogen) electrodes substrate, and employ electrocatalytically active oxygen electrodes. Unfortunately, a direct use of active oxygen electrodes such as perovskite structured cobaltites[3–5] in SOCs has been proven formidable due to their reaction with ZrO_2-based electrolytes and much higher thermal expansion efficient than the electrolytes. To address the first problem, applying a CeO_2-based barrier layer between electrolytes and oxygen electrodes is needed.[6] However, introduction of such a barrier layer considerably increases the ohmic resistance (sometimes as high as 2–3×), thus defeating the purpose of enhancing cell performance. To address the second problem, mixing the active oxygen electrode with CeO_2-based material or infiltrating it into a thermally compatible skeleton is currently the solution, but a CeO_2-based barrier layer is still needed in this case.

Therefore, a key development for ZrO_2-based IT-SOCs is to find an active oxygen electrode without the need of a barrier layer. Here we show that a composite consisting of $La_{0.8}Sr_{0.2}MnO_3$ (LSM), an excellent electronic conductor, and $(Bi_{0.75}Y_{0.25})_{0.93}Ce_{0.07}O_{1.5\pm\delta}$ (BYC), an excellent oxide-ion conductor, is a potential barrier layer free (BLF) oxygen electrode for IT-SOCs. We also show phase inversion fabrication of open structured hydrogen electrode substrate to facilitate H_2/H_2O diffusion.

Experimental

Material synthesis.—The $(Bi_{0.75}Y_{0.25})_{0.93}Ce_{0.07}O_{1.5\pm\delta}$ (BYC) and $La_{0.8}Sr_{0.2}MnO_3$ (LSM) powders were separately synthesized by citric acid (CA)-nitrate method.[7,8] For BYC powder, CA, and stoichiometric amounts of metal nitrate precursors (mole ratio of 1.5:1 for CA and total metal ions) were first dissolved into a diluted nitric acid solution (volume ratio of concentrated nitric acid to deionized (DI) water is 1:9). The solution was then heated at 80 °C to condense the solution, followed by heating to 200 °C for auto-combustion. Finally, the collected powder was calcined at 700 °C for 4 h. For making LSM powder, it followed a similar process, but pH of the nitrate solution was adjusted to ∼6 with ammonia (28%–30%). The collected powder was calcined at 900 °C for 5 h. The phase purity of the powders was examined by an X-ray diffractometer (XRD, Rigaku) equipped with graphite-monochromatized Cu Kα radiation (λ = 1.5418 Å) over a 2θ range of 10°–80° in a step size of 5°·min^{-1}.

Fabrication of symmetrical cell and single cells.—To evaluate the performance of LSM/BYC oxygen electrode (OE), a symmetrical cell with $(Sc_2O_3)_{0.1}(CeO_2)_{0.01}(ZrO_2)_{0.89}$ (ScSZ, Daiichi Kigenso Kagaku Co. Ltd., Japan) as electrolyte and LSM/BYC as two symmetrical OEs. The ScSZ electrolyte with a thickness of 150 μm was prepared by tape casting method.[9] In brief, ScSZ powders were mixed with toluene, ethanol, and fish oil in a planetary mill for 24 h. Then, polyvinyl butyral (PVB, Sigma–Aldrich) as a binder and DOP (Dioctyl phthalate, Acros Organics) as a plasticizer were added into the above slurry and milled for another 24 h. The casted green tape was dried in air for 24 h. The next step was to laminate the ScSZ tape by hot-pressing. The as pressed tape was then cut into discs, and finally sintered at 1350 °C for 5 h in air. The OE slurry was prepared by mixing LSM, BYC and V-006A (in a weight ratio of 60:40:100), and then was screen-printed onto the two surfaces of the ScSZ electrolyte. The OE was finally fired at 800 °C for 2 h.

Two types of hydrogen electrode (HE) supported single cells have been prepared using tape-casting method (denoted as HE-TC) and phase-inversion method (denoted as HE-PI).[10] The slurry for HE-TC has a solid weight ratio of NiO:ScSZ:Graphite = 60:40:30, and it uses the same tape casting method as ScSZ symmetric cell. The slurry for HE-PI has a solid weight ratio of NiO:ScSZ:Graphite = 60:40:10 using Polyethersulfone (PESF, Ameco Performance® Radel

*Electrochemical Society Member.
[z]E-mail: huang46@cec.sc.edu

A-300) and polyvinylpyrrolidone (PVP, Sigma-Aldrich) as binder, and 1-methyl-2 pyrrolidone (NMP, Sigma-Aldrich) as solvent. The slurry was then cast on a flat glass plate and immersed into DI water for 10 h to finish the exchange process. Both the green tapes of HE-TC and HE-PI were heated to 600 °C at a rate of 1 °C min^{-1} and held for 1 h to remove graphite and other organic materials, followed by heating to 1000 °C at a rate of 2 °C min^{-1} and holding for 2 h. A NiO/ScSZ functional layer (~15 μm, NiO:ScSZ = 60:40 in weight) and ScSZ electrolyte layer (~10 μm) were subsequently dip-coated on the HE-support, followed by sintering at 1350 °C for 5 h. The LSM/BYC ink was last screen-printed onto the surface of ScSZ, followed by firing at 800 °C for 2 h. For all the cells used in this work, the geometric area of the LSM/BYC OE was fixed at 0.4 cm^2. We typically test 2–3 replicates for each type of cell to ensure the repeatability of the results. The results showed are representative of the group.

Symmetrical cell characterization using 3-electrode method.—To evaluate the overpotentials contributed from different cell components, we used the symmetrical three-electrode cell (STEC) method; the detail on this method can be found in previous Ref. 11. Figure 1 shows a schematic of STEHC. The counter electrode (CE) and working electrode (WE) are identical OE of LSM-BYC, while the reference electrode (RE) is a gold wire attached to the circumference of the electrolyte disk. Depending on the direction of the DC current applied, EIS spectrum related to either ORR or OER polarization can be obtained. The temperature of interest for this study was ranged from 500 °C to 650 °C in a 50 °C interval. The obtained polarization resistance (R_p) is then integrated over current density (J) to obtain overpotential (η).

Full cell testing.—For full cell testing, silver wire/mesh together with gold paste was used as current collectors for both electrodes and fired at 700 °C. The button cell with the current collector was then glass sealed to an alumina tube. The cell was first heated up to 650 °C with HE exposing to 4%H_2-N_2 and OE exposing to air; HE gas was then switched to wet 3%H_2O-H_2 with a flow rate of 50 ml·min^{-1}, allowing a reduction of NiO to Ni. Next, electrochemical performance of the single cell was tested at the same H_2 flow rate but with different H_2O contents: 3, 10, 20 and 30% H_2O. A steamer with a syringe pump was used to vary the steam content. EIS and I–V polarization curves were measured using an electrochemical workstation (Solartron 1470E/FRA1255 Multi-Channel System). EIS spectra were measured under open circuit voltage (OCV) as well as loaded conditions, and frequency sweeping from 100 kHz to 0.01 Hz at an amplitude of 10 mV. The stability of the cell was evaluated at 650 °C by recording the output current under a constant electrolysis voltage (1.3 V). Microstructures of the cell were examined with a scanning electron microscopy (SEM, Zeiss Gemini 500 FESEM, Germany) equipped with energy dispersive spectroscopy (EDS).

Result and Discussion

Phase composition of LSM/BYC.—The XRD patterns of LSM, BYC and LSM/BYC are shown in Fig. 2. No sign of impurity is found in LSM, BYC and LSM/BYC. The BYC is identified as a cubic fluorite structure with space group of Fm-3m, indicating that the high-temperature δ-Bi_2O_3 cubic phase has been stabilized to room temperature by Ce- and Y- co-doping. Our previous study has shown that BYC has an oxide-ion conductivity of σ_0 = 0.1 S·cm^{-1} at 650 °C without degradation for over 300 h,[12] which is highly desirable for IT-SOFCs. After BYC was mixed with LSM and calcined at 800 °C for 2 h, no reaction between LSM and BYC is found, indicating good chemical compatibility between them.

Determining OER and ORR polarization kinetics.—To determine the area specific resistances (R_p) related to OER and ORR processes, we employed STEHC method schematically shown in

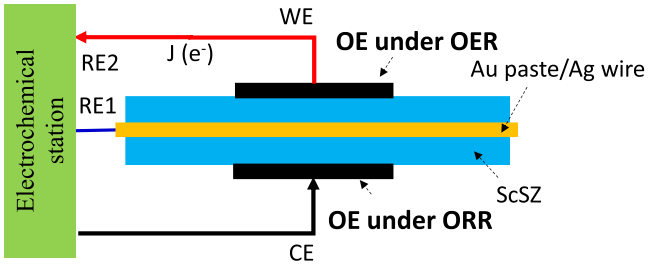

Figure 1. Schematic of experimental setup for three-electrode symmetrical cell.

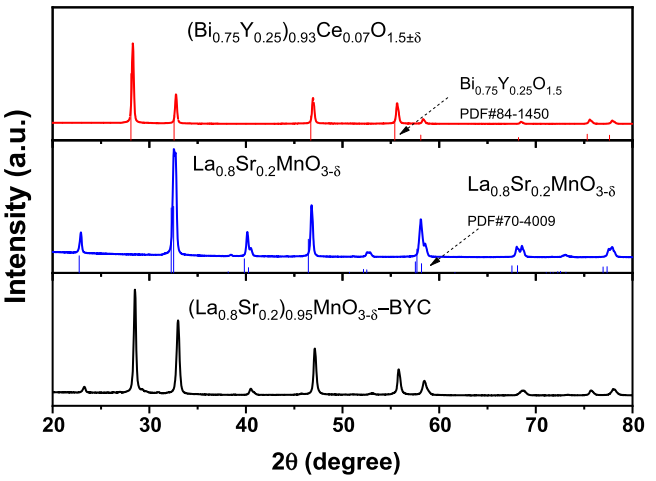

Figure 2. XRD patterns of synthesized BYC, LSM and LSM/BYC at 700, 900 and 800 °C, respectively.

Fig. 1; the results are shown in Fig. 3. As expected from Butler-Volmer's charge transfer theory, Fig. 3a shows that R_p decreases with current density (J) at each temperature, either in OER or ORR mode. The degree of R_p reduction is more pronounced at lower temperatures, further implying the low-temperature dominance of charge transfer process. At higher temperatures where charge-transfer process is activated, J has less effect on R_p. It is interesting to mention that OER-R_p of the BLF-OE becomes noticeably lower than that of ORR at high J, see Fig. 3a, making the polarization curve asymmetrical. This finding is important evidence that BLF-OE is a better OER electrode at high J, providing a better rate of oxygen release to mitigate delamination. Similarly, overpotential (η) derived from R_p in Fig. 3b shows a typical Tafel curve in both OER and ORR domains, from which exchange current density (i_o) and transfer coefficient (α) can be obtained by fitting experimental data using Butler–Volmer equation[13] (assuming that ORR and OER are multi-step charge transfer processes, but the rate-limiting step involves only single electron transfer) with i_o and α as variables

$$i = i_o\left(\exp\left(\frac{(1-\alpha)F\eta}{RT}\right) - \exp\left(-\frac{\alpha F\eta}{RT}\right)\right) \quad [1]$$

where F, R and T have their usual meanings. The fitting results are shown in Fig. 3c as a function of temperature. It is clear that i_o follows Arrhenius relationship with T with activation energy E_a = 1.06 eV, while $\alpha \approx 0.35$ remains nearly independent of temperature. The latter is reasonable since the polarization curve is asymmetrical ($\alpha \neq 0.5$) and remains the same for every temperature.

Figure 4 shows a short-term stability of R_p and R_o (ohmic resistance) at 1 A cm^{-2} and 650 °C in both OER and ORR modes. Figures 4a and 4b indicates that R_p and R_o remain rather stable during ORR, suggesting LSM/BYC is a stable OE for fuel cell mode.

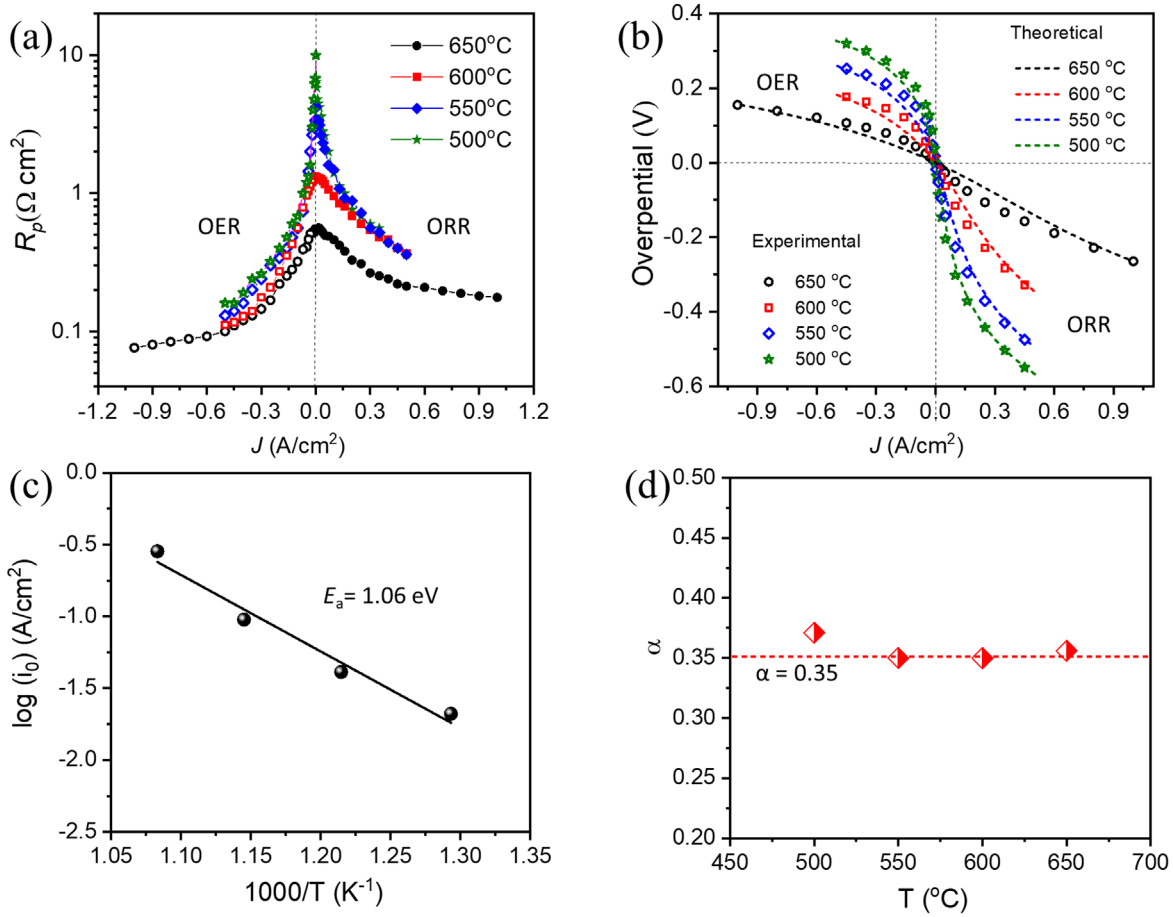

Figure 3. (a) R_p vs J at different temperatures; (b) the corresponding overpotential (η) vs J at different temperatures; (c) log (i_0) and (d) α vs T.

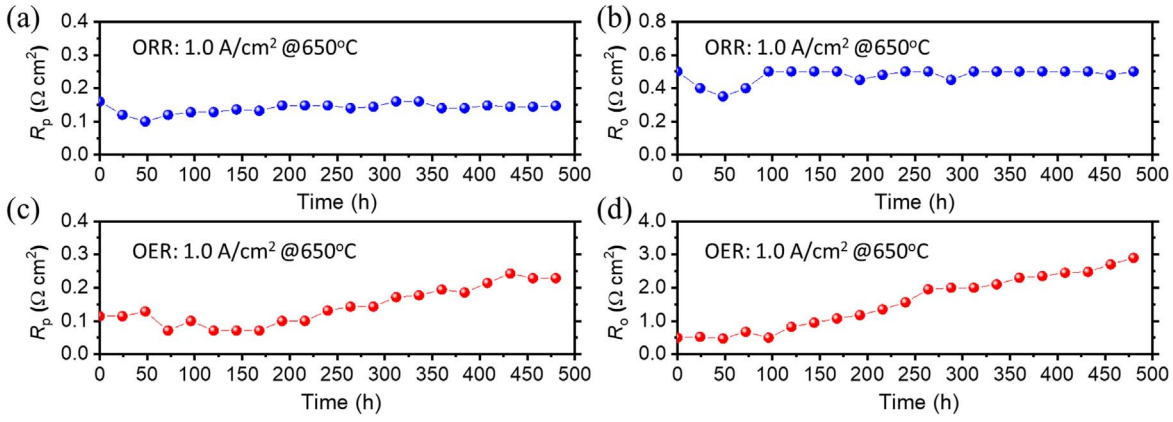

Figure 4. Short-term stability of R_p at 1 A cm^{-2} and 650 °C under both OER and ORR modes.

However, in OER mode, Fig. 4c shows that R_P begins to increase after 200 h, and approaches to 0.25 Ω·cm^2 after 500 h from the initial value of 0.10 Ω·cm^2. In the meanwhile, Fig. 4d shows a pronounced increase in R_o, from 0.5 to 3.0 Ω·cm^2 over 500 h. We think that this increase in R_p and R_o during OER polarization is related to the delamination of OE.

To verify the OE delamination, SEM images of samples after testing were acquired. Figures 5c and 5e show the cross-sectional SEM images of the OE after the ORR and OER stability tests. For OE tested in ORR mode, there is no sign of delamination at the interface, but a thin layer of concentrated Bi_2O_3 is seemingly present at the interface with ScSZ electrolyte, see Fig. 5d. Since this thin layer was not found in the fresh OE, see Fig. 5(a), it implies that the applied ORR current may have caused it. Similar phenomenon has also been reported in LSM/$Bi_{1.6}Er_{0.4}O_3$ (ESB) OE,[14,15] where a continuous nanoscale ESB layer (ca. 50 nm) was reported to self-assemble at the cathode/electrolyte interface. This could be related to the Joule heating at the interface under high current, which could drive Bi_2O_3 diffusion because of its low melting temperature. Nevertheless, the formed Bi_2O_3 layer does not seem to have negative effect on the stability of OE; it may in fact enhance bonding and oxide-ion transfer. For the OE tested in OER mode, see Figs. 5e and 5f, there is no Bi_2O_3 layer formed at the interface, but delamination is clearly seen, which contributes to R_o and R_p

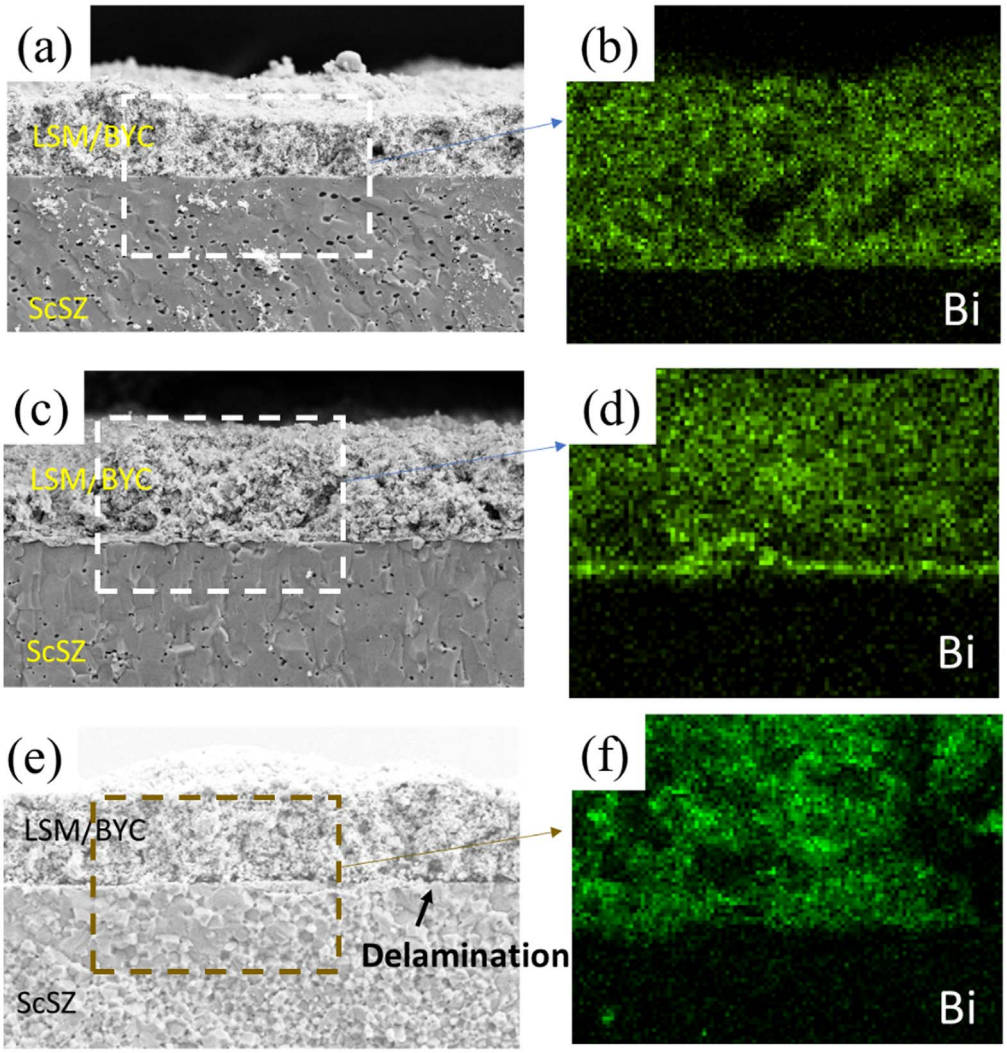

Figure 5. SEM images and EDS mapping of LSM/BYC OE: (a) and (b) as-sintered 3-electrode; (c) and (d) after 3-electrode ORR testing; (e) and (f) after 3-electrode OER testing.

increases during the test. The delamination is mainly related to the high local oxygen partial pressure built up at the interface during OER polarization under high current.[16] To avoid the delamination, one should lower η by reducing applied J or R_p.

Electrochemical performance of full SOC.—Full SOCs with BLF-OE and two types of HE supports (HE-TC and HE-PI) were tested under both fuel cell and electrolyzer modes. To minimize variables, the two HE supports have the same thickness (~400 μm). Figure 6 compares the cross-sectional microstructures of the HE-TC and HE-PI substrates before H_2-reduction. Evidently, HE-PI substrate contains more open straight pores than HE-TC counterpart. The overall structure contains three layers: a thick layer with large finger-like channels for bulk gas diffusion, a porous spongy-like layer with a thickness of ~50 μm and a thin 10 μm functional layer with fewer pores.

In comparison, the HE-TC substrate has two distinct layers, i.e. a thick and porous support layer with random pores and a thin functional layer. It is noted that the close pores in HE-PI substrate derived from 10 wt% graphite pore former, are uniform and have a better sphericity, even though it is lower than 30 wt% used in HE-TC. This could be due to the different preparation processes of the HE slurry, for example, the graphite may be crushed during the TC slurry preparation process.

Figures 7a and 7b show the I–V–P curves and EIS spectra for the HE-TC and HE-TC cells with the LSM/BYC BLF-OE. In Fig. 7a, the peak power density reaches 0.8 W cm^{-2} at 650 °C. The performance is higher than 0.45 W cm^{-2} of our previously tested cell with HE and electrolyte fabricated by uniaxial co-pressing method,[8] and comparable to the best reported results using HE supported cells with other LSM-Bi_2O_3 composites as OE.[17,18] But the cell still has room to improve. For example, our previous study has shown that LSM/BYC OE using a one-pot method can further reduce R_o and R_p.[19]

In comparison, the HE-PI cell exhibits a peak power density of 0.5 W cm^{-2} at 650 °C. From the EIS spectrum shown in Fig. 7b, R_o of the HE-PI cell is 0.1 $\Omega \cdot cm^2$, the same as the HE-TC cell. Thus, the lower power density of HE-PI cell is mainly caused by the larger polarization resistance related to the HE since the two cells have the same OE. As shown in Nyquist plot, HE-PI cell has a polarization resistance of 1.4 $\Omega \cdot cm^2$, higher than the HE-TC cell (0.9 $\Omega \cdot cm^2$). From the Bode plot, the HE-PI cell has a larger resistance than the HE-TC cell at the intermediate frequency range. To further identify the cause of the observed performance difference, we perform a distribution of relaxation times (DRT) analysis on EIS spectra,[20] and the results are shown in Fig. 7c. Six peaks labeled as P1 to P6 are distinguishable in DRT diagram for both cells. The DRT resistance of P4 for HE-PI cell is noticeably higher than HE-TC cell in the

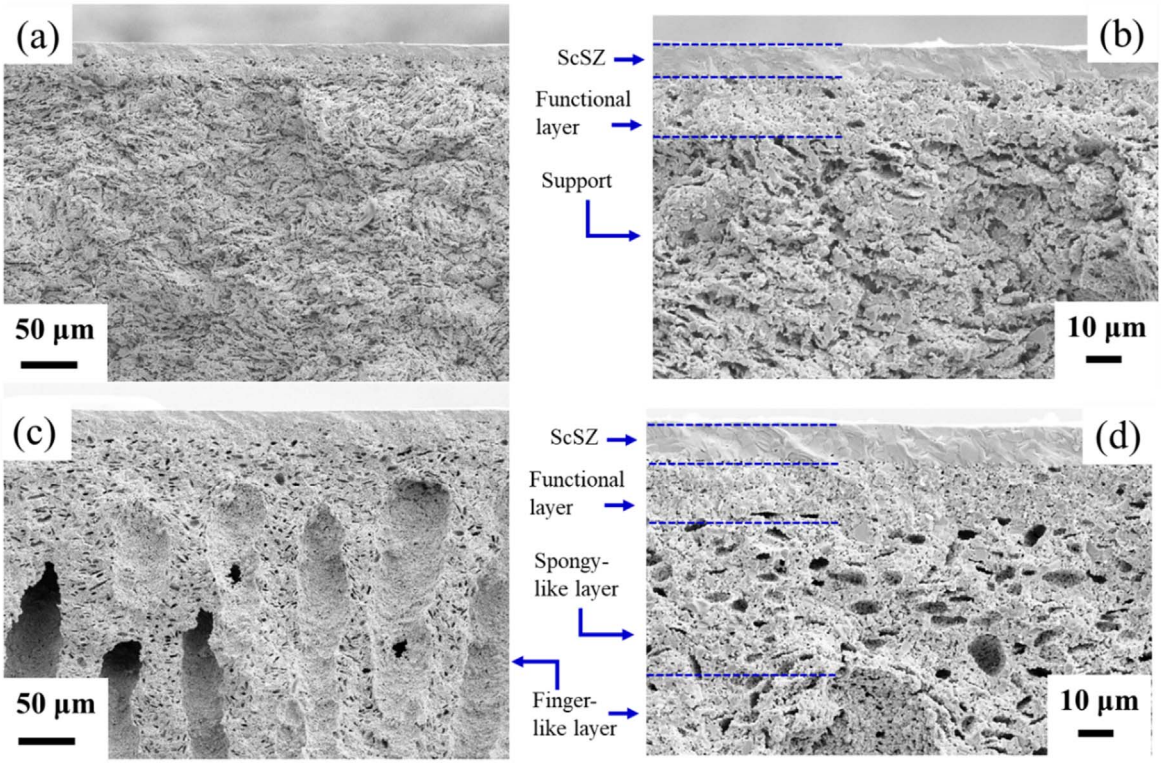

Figure 6. SEM images of (a) and (b) TC-derived HE substrate before reduction; (c) and (d) PI-derived HE substrate before reduction.

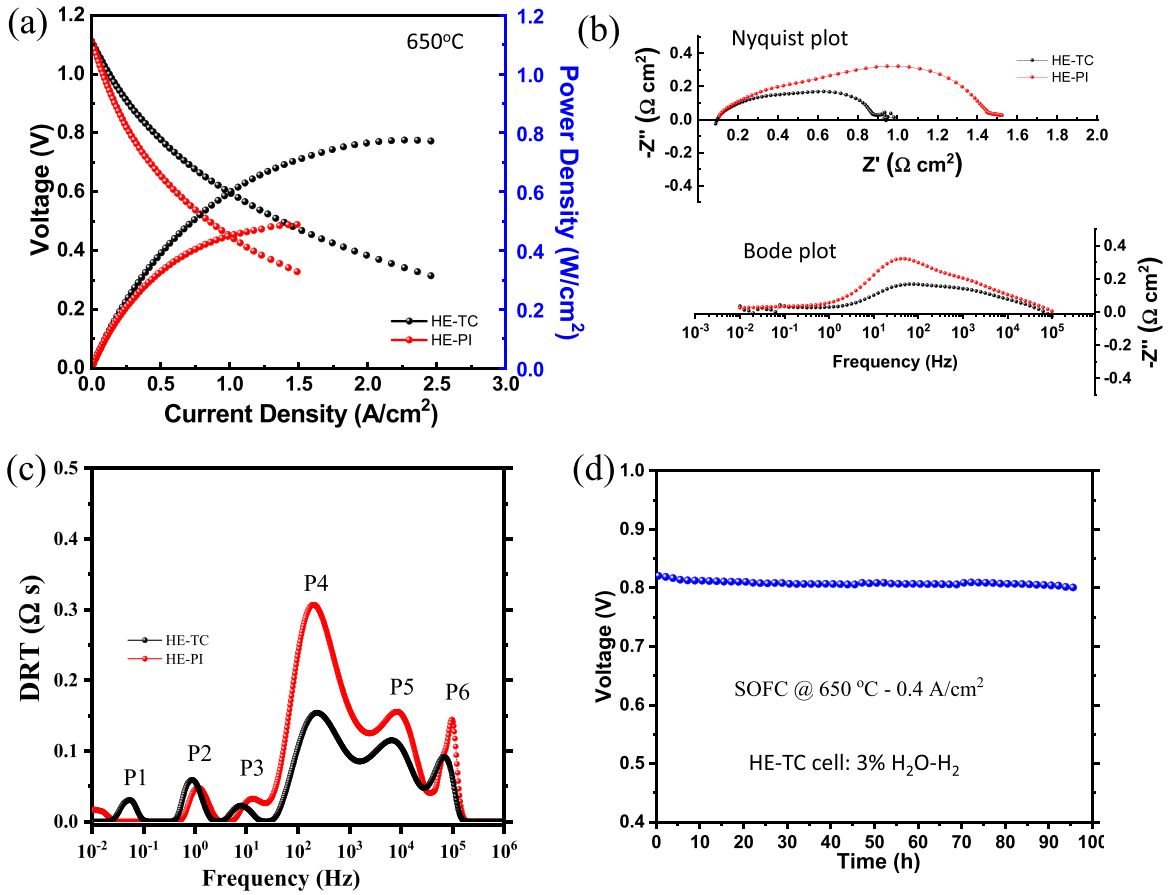

Figure 7. Comparison between HE-PI and HE-TC cells at 650 °C. (a) V–I–P curve; (b) EIS spectra under OCV; (c) DRT diagram; and (d) stability of HE-TC cell in fuel cell mode.

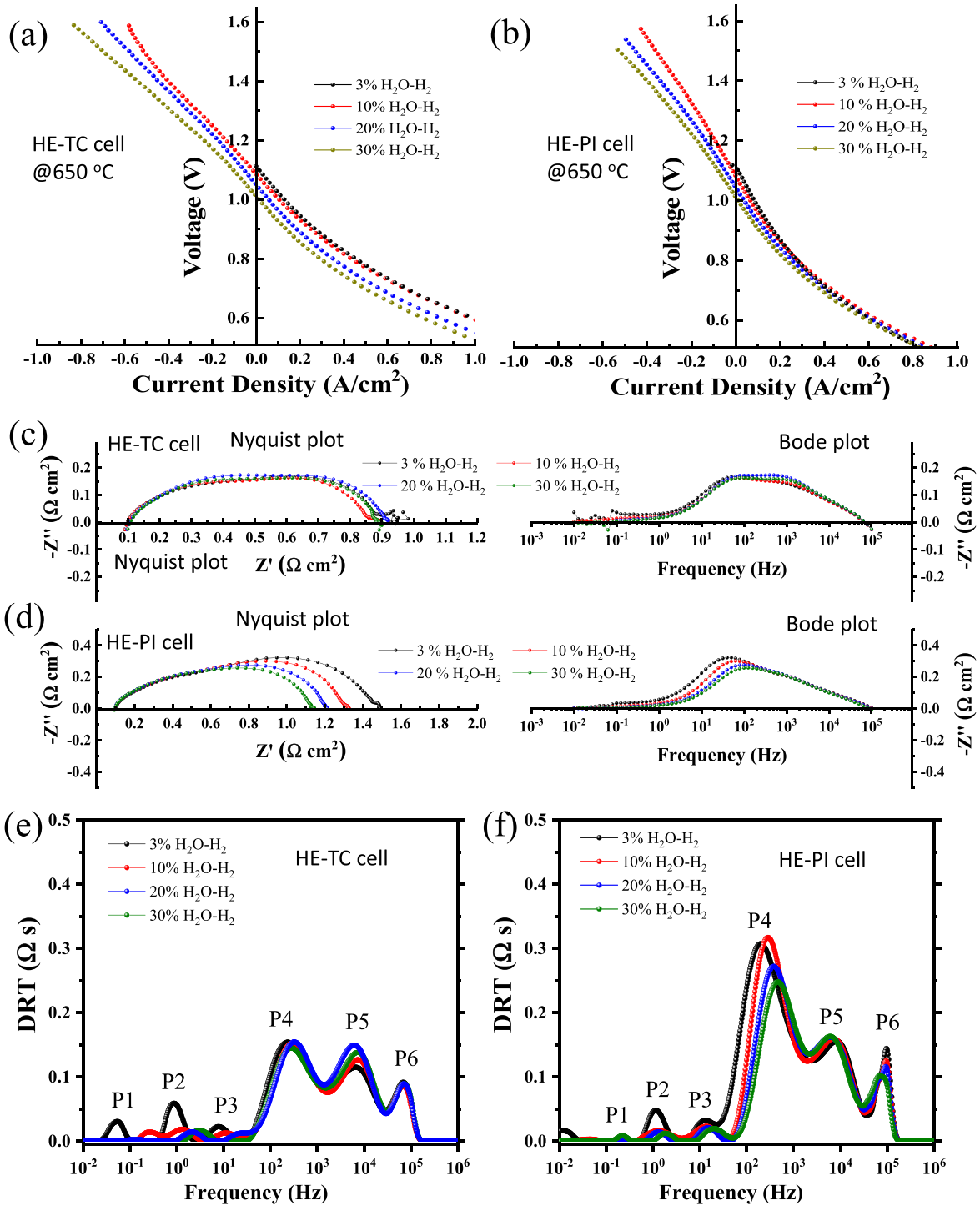

Figure 8. The effect of H_2O contents on V–I curve of (a) HE-TC cell and (b) HE-PI cell; EIS spectra of (c) HE-TC cell and (d) HE-PI cell; DRT diagrams of (e) HE-TC cell and (f) HE-PI cell.

frequency range of $10^2 \sim 10^3$ Hz, which is typically associated with the mass transfer process (e.g., adsorption/desorption, dissociation, and surface diffusion). P5 and P6 located in the frequency range of $10^4 \sim 10^5$ Hz, which are related to the charge transfer at three-phase-boundaries (TPBs), are also higher for HE-PI cell, indicating TPBs for HE-PI are less than HE-TC. On the other hand, P1 ∼ P3 for the HE-PI cell in the frequency range of $10^{-2} \sim 10^1$Hz, which are associated with gas diffusion process, are slightly lower than the HE-TC cell, suggesting that the HE-PI cell has a low-resistance structure for gas diffusion. Therefore, lower performance of the HE-PI cell could be resulted from its fewer active sites for H_2 oxidation; its gas diffusion resistance does not show up due to its open microstructure.

The laboratory short-term performance stability of HE-TC cell operated under fuel cell mode is particularly shown in Fig. 7d due to its better performance than HE-PI cell; no sign of degradation is seen for ∼100 h under 0.4 A cm^{-2} and 3% H_2O-H_2 at 650 °C. Longer testing is needed for future study.

Figures 8a and 8b show V–I curve comparison of HE-TC and HE-PI cells in both fuel cell and electrolyzer domains under different H_2O-H_2 conditions at 650 °C. For both cells, OCVs are 1.11, 1.08,

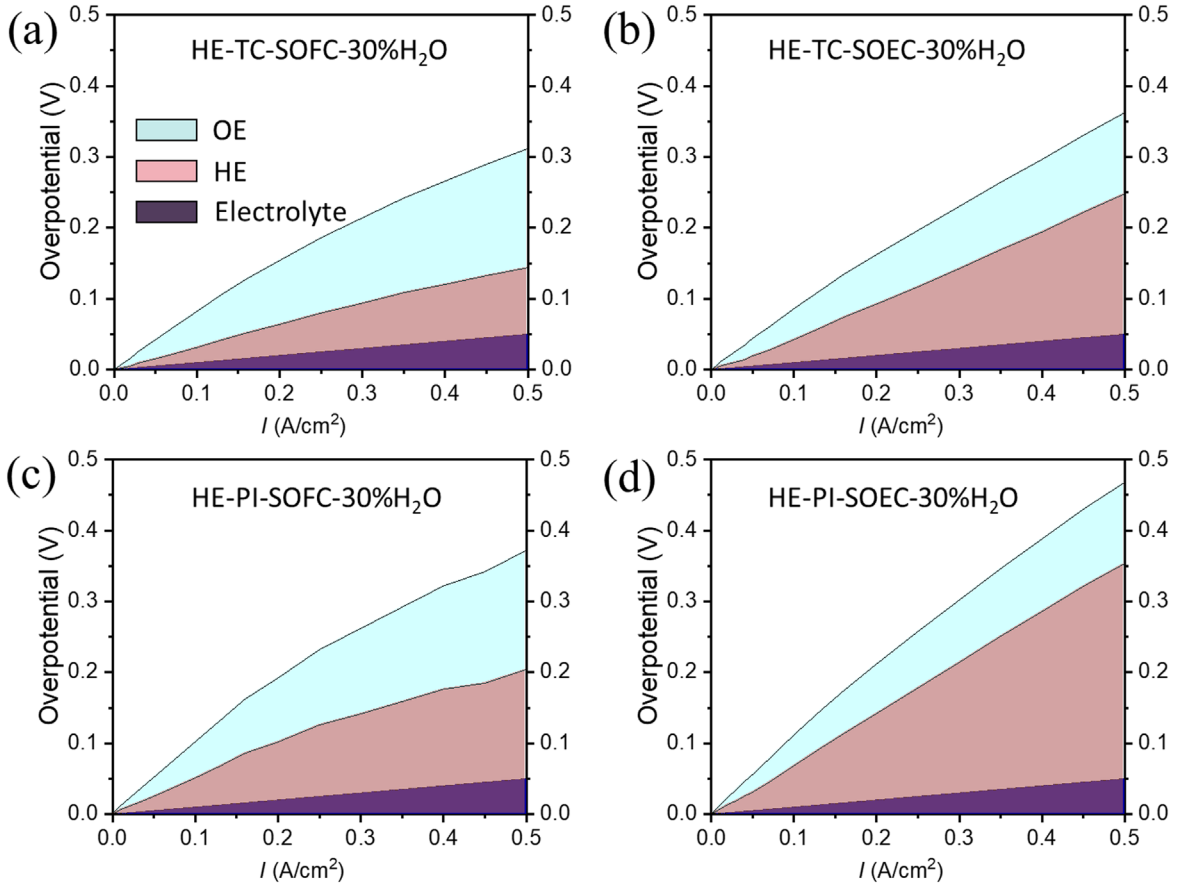

Figure 9. Overpotential distributions of HE-TC cell in (a) fuel cell and (b) electrolyzer, and HE-PI cell in (c) fuel cell and (d) electrolyzer.

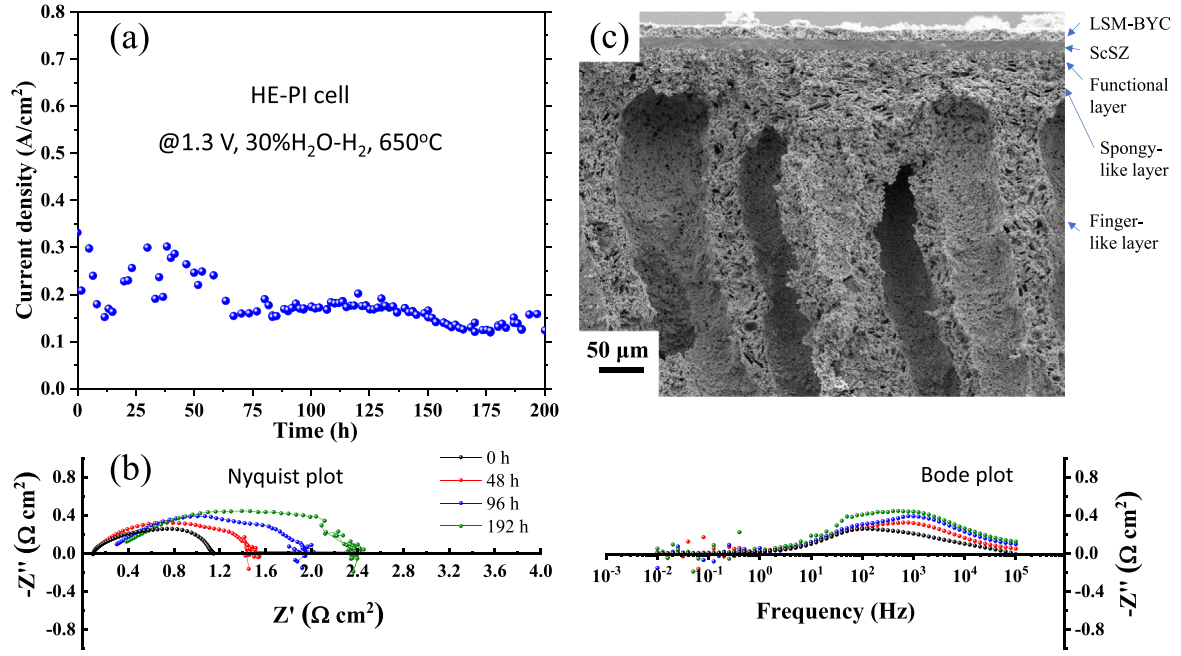

Figure 10. (a) Stability of a HE-PI cell tested under 30%H_2O-H_2, 1.3 V and 650 °C; (b) EIS spectra vs time; (c) microstructure of the HE-PI cell after testing.

1.05 and 1.00 V for 3, 10, 20 and 30% H_2O in H_2, respectively; these values are very close to the theoretical ones (1.128, 1.077, 1.045 and 1.023 V for 3, 10, 20 and 30% H_2O in H_2, respectively), suggesting that the cells are well-sealed and the electrolyte is dense enough. It is noted that HE-TC cell appears to have a stronger concentration polarization than HE-PI cell under electrolyzer mode under the condition of high J and 10%H_2O-H_2, implying that the ratio of porosity to tortuosity (ε/τ) in the HE-TC substrate might be a little bit low for 10%H_2O transport. Nevertheless, as H_2O content increases, the concentration polarization becomes reduced. For the

HE-PI cell, however, in all cases, the electrolyzer voltage is approximately linear with J, and no sign of strong concentration polarization is observed. Thus, the HE-PI open structure is indeed beneficial to H_2O transport, especially when the stream concentration is low. However, the HE-PI cell did not outperform the HE-TC cell as expected; its electrolysis J at 1.3 V is only 0.28 A cm^{-2} at 30% H_2O-H_2 vs 0.40 A cm^{-2} for the HE-TC cell. While ε/τ in the two HE-substrates are sufficient for high H_2O concentrations, what makes the performance difference could be the density of reactive sites.

The effect of H_2O contents on cell polarization was also studied by combined EIS and DRT analysis. Figures 8c and 8d show EIS spectra of the two cells. Clearly, the two cells have the same R_o = 0.1 $\Omega \cdot cm^2$, but different R_p. The H_2O concentration has almost no effect on R_p of HE-TC cell, whereas it is significant to the HE-PI cell. Figures 8e and 8f of DRT charts further confirm the H_2O effect.

For the HE-PI cell, one can see that an increase in H_2O content reduces R_p and shifts the spectrum to higher frequency with reduced DRT resistance. The DRT resistance changes mainly occur at P4 and P6, which are mainly associated with mass and charge transfer processes, suggesting that H_2O-related concentration polarization might be an issue. We acknowledge the 50 μm thick spongy layer (see Fig. 6d) between the functional layer and the substrate could be problematic because its pores are not well connected (high τ), see Fig. 6d. For the HE-TC cell, the insensitivity of R_p on H_2O content implies that the cell is not mass transport limited and possesses sufficient reactive sites for H_2O splitting.

Overpotential distribution in HE and OE.—Based on the I–V curves of full cells and η–J curves of OE only (Fig. 3), we can further separate total η of the full cell into that of OE, HE, and electrolyte. We take the I–V curve under 30% H_2O-H_2 condition as an example; the results are shown in Fig. 9. In all cases, voltage loss caused by the electrolyte is the same, because R_o remains constant (0.1 $\Omega \cdot cm^2$) at different J for the two types of cells. Thus, we can focus on η of OE and HE. For the HE-TC cell, it seems that OE dominates the full cell performance under fuel cell mode, while HE dominates under electrolyzer mode. This is because H_2 oxidation in HE is faster and easier under fuel cell, and HE-TC substrate can provide sufficient active sites for the reaction. In electrolyzer mode, however, the kinetics of H_2O splitting is relatively slow, especially when the microstructure does not fully favor gas transport. For the HE-PI cell, it generally has a similar trend to the HE-TC cell, i.e. HE makes a greater contribution to the whole η in electrolyzer mode. Although the HE-PI substrate has a better pore structure, it fails to provide sufficient active sites for fuel cell and electrolyzer operations. Overall, the current design of HE-PI substrate needs further improvement in order to balance electrocatalytic and gas transport performances for electrolyzer operation.

The short-term stability (J@1.3 V) of the HE-PI cell operated under electrolyzer mode is shown in Fig. 10. The overall voltage fluctuation is largely caused by the unstable H_2O supply with our self-made steamer. Clearly, this needs to be improved for future testing. At the beginning of the testing, J generally matches Fig. 8b under the same condition, even though it is still oscillating. After 75 h, electrolyzer J appears to be stabilized at a lower J, which is possibly due to a change in H_2O content caused by the unstable steamer and fuel line condensation. During this period, Fig. 10b of EIS spectra indicates mainly a gradual increase in R_p, not necessarily R_o. Therefore, the degradation is not likely associated with OE delamination, particularly at such a low J.

Figure 10c shows microstructure of the cell after testing. There is virtually no change in microstructure compared to that of before testing (Fig. 6). Therefore, we speculate that the current-density degradation and fluctuation shown are possibly related to the unstable steam supply and fuel line condensation. Clearly, we need to improve the steamer performance in the future.

Conclusions

In summary, we have investigated a barrier layer free oxygen electrode (BLF-OE) and open structured hydrogen electrode (HE) for IT-SOCs. The results show that LSM/BYC BLF-OE exhibits good oxygen electrocatalytic activity toward both OER and ORR at IT range (<700 °C). However, at high OER current density (1 A cm^{-2}), it starts to show delamination after 200 h. Lowering operating current density or R_p can mitigate or delay the delamination. A further analysis of overpotential distribution among cell components indicates that OE and HE account for major voltage loss under fuel cell and electrolyzer modes, respectively. From HE substrate study, the results show that PI-derived HE exhibits slightly lower concentration polarization but relatively higher activation polarization than its TC-derived counterpart. The TC-derived cell generally outperforms PI-derived cell in both fuel cell and electrolyzer modes due to its higher density of the reactive sites. Further improvement in HE-PI cells with balanced concentration and activation polarization is needed to further boost the overall performance. We also show the necessity to further improve steamer performance and fuel line heating in our future testing.

Acknowledgments

This material is based upon work supported by the U.S. Department of Energy's Office of Energy Efficiency and Renewable Energy (EERE) under the Fuel Cell Technologies Office (FCTO) under Award Number DE-EE-0008842 and Office of Fossil Energy and Carbon Management under National Energy Technology Lab under award number DE-FE-32111.

ORCID

Kevin Huang https://orcid.org/0000-0002-1232-4593

References

1. S. D. Ebbesen, S. H. Jensen, A. Hauch, and M. B. Mogensen, *Chem. Rev.*, **114**, 10697 (2014).
2. Z. Gao, L. V. Mogni, E. C. Miller, J. G. Railsback, and S. A. Barnett, *Energy Environ. Sci.*, **9**, 1602 (2016).
3. L. Dieterle, D. Bach, R. Schneider, H. Störmer, D. Gerthsen, U. Guntow, E. Ivers-Tiffée, A. Weber, C. Peters, and H. Yokokawa, *J. Mater. Sci.*, **43**, 3135 (2008).
4. F. Figueiredo, J. Labrincha, J. Frade, and F. Marques, *Solid State Ionics*, **101**, 343 (1997).
5. K. Lee and A. Manthiram, *J. Electrochem. Soc.*, **153**, A794 (2006).
6. R. Knibbe, J. Hjelm, M. Menon, N. Pryds, M. Søgaard, H. J. Wang, and K. Neufeld, *J. Am. Ceram. Soc.*, **93**, 2877 (2010).
7. C. Zhang and K. Huang, *ACS Energy Lett.*, **1**, 1206 (2016).
8. C. Zhang and K. Huang, *J. Power Sources*, **342**, 419 (2017).
9. R. K. Nishihora, P. L. Rachadel, M. G. N. Quadri, and D. Hotza, *J. Eur. Ceram. Soc.*, **38**, 988 (2018).
10. C. Jin, C. Yang, and F. Chen, *J. Membr. Sci.*, **363**, 250 (2010).
11. X. Jin and K. Huang, *J. Electrochem. Soc.*, **167**, 124501 (2020).
12. K. Huang, M. Feng, and J. B. Goodenough, *Solid State Ionics*, **89**, 17 (1996).
13. A. J. Bard and L. R. Faulkner, *Electrochemical Methods*, **2**, 580 (2001).
14. K. T. Lee, A. A. Lidie, H. S. Yoon, and E. D. Wachsman, *Angew. Chem. Int. Ed.*, **53**, 13463 (2014).
15. M. Chen, Y. Cheng, S. He, N. Ai, J.-P. Veder, W. D. Rickard, M. Saunders, K. Chen, and T. Zhang, *J. Power Sources*, **397**, 16 (2018).
16. B.-K. Park, Q. Zhang, P. W. Voorhees, and S. A. Barnett, *Energy Environ. Sci.*, **12**, 3053 (2019).
17. M. Chen, Y. Cheng, S. He, N. Ai, J.-P. Veder, W. D. A. Rickard, M. Saunders, K. Chen, T. Zhang, and S. P. Jiang, *J. Power Sources*, **397**, 16 (2018).
18. B.-H. Yun, K. J. Kim, D. W. Joh, M. S. Chae, J. J. Lee, D.-W. Kim, S. Kang, D. Choi, S.-T. Hong, and K. T. Lee, *J. Mater. Chem. A*, **7**, 20558 (2019).
19. W. Fang, T. Yang, and K. Huang, *Chem. Commun.*, **55**, 2801 (2019).
20. T. H. Wan, M. Saccoccio, C. Chen, and F. Ciucci, *Electrochim. Acta*, **184**, 483 (2015).